Bioactive Materials 47 (2025) 18–31

Contents lists available at ScienceDirect

Bioactive Materials

journal homepage: www.keaipublishing.com/en/journals/bioactive-materials

Bioaugmented design and functional evaluation of low damage implantable array electrodes

Ling Wang [a,b,*,1], Chenrui Zhang [a,b,1], Zhiyan Hao [a,b,c,1], Siqi Yao [a,b], Luge Bai [a,b], Joaquim Miguel Oliveira [d,e], Pan Wang [f], Kun Zhang [g], Chen Zhang [h], Jiankang He [a,b], Rui L. Reis [d,e], Dichen Li [a,b,**]

[a] State Key Laboratory for Manufacturing System Engineering, School of Mechanical Engineering, Xi'an Jiaotong University, China
[b] State Industry-Education Integration Center for Medical Innovations, Xi'an Jiaotong University, China
[c] Department of Intelligent Manufacture, Yantai Vocational College, 264670, China
[d] 3B's Research Group, I3Bs – Research Institute on Biomaterials, Biodegradables and Biomimetics, University of Minho, Headquarters of the European Institute of Excellence on Tissue Engineering and Regenerative Medicine, AvePark, Zona Industrial da Gandra, Barco, 4805-017, Guimarães, Portugal
[e] ICVS/3B's - PT Government Associate Laboratory, Braga/Guimarães, Portugal
[f] Department of Anatomy, Histology and Embryology and K.K. Leung Brain Research Centre, The Fourth Military 9 Medical University, 710032, Xi'an, China
[g] Department of Pharmacology, School of Pharmacy, Fourth Military Medical University, Xi'an, 710032, China
[h] Tianjin Medical Devices Quality Supervision and Testing Center, Tianjin, 300384, China

ARTICLE INFO

Keywords:
Implantable neural electrodes
Bioaugmented design
Biocompatibility
Scar tissue suppression
Signal-to-noise ratio

ABSTRACT

Implantable neural electrodes are key components of brain-computer interfaces (BCI), but the mismatch in mechanical and biological properties between electrode materials and brain tissue can lead to foreign body reactions and glial scarring, and subsequently compromise the long-term stability of electrical signal transmission. In this study, we proposed a new concept for the design and bioaugmentation of implantable electrodes (bio-array electrodes) featuring a heterogeneous gradient structure. Different composite polyaniline-gelatin-alginate based conductive hydrogel formulations were developed for electrode surface coating. In addition, the design, materials, and performance of the developed electrode was optimized through a combination of numerical simulations and physio-chemical characterizations. The long-term biological performance of the bio-array electrodes were investigated *in vivo* using a C57 mouse model. It was found that compared to metal array electrodes, the surface charge of the bio-array electrodes increased by 1.74 times, and the impedance at 1 kHz decreased by 63.17 %, with a doubling of the average capacitance. Long-term animal experiments showed that the bio-array electrodes could consistently record 2.5 times more signals than those of the metal array electrodes, and the signal-to-noise ratio based on action potentials was 2.1 times higher. The study investigated the mechanisms of suppressing the scarring effect by the bioaugmented design, revealing reduces brain damage as a result of the interface biocompatibility between the bio-array electrodes and brain tissue, and confirmed the long-term *in vivo* stability of the bio-array electrodes.

1. Introduction

Brain is one of the most complex systems within an organism, comprising hundreds of billions of neurons that form extensive neural networks. Brain-computer interface (BCI) technology can facilitate the bidirectional transmission of neural signals and device interactions by connecting with the brain, thus playing a crucial role in long-term objectives such as understanding, controlling, and developing the brain [1]. Invasive BCI systems, which employ surgically implanted neural electrodes, are aimed to capture high-quality neural signals and enable in-depth studies at the cellular level [2–4]. The most commonly used implantable neural electrodes include cost-effective microwire electrodes, semiconductor-based silicon electrode arrays, such as Utah arrays, and the linear microelectrode arrays known as Michigan electrodes

* Corresponding author. State Key Laboratory for Manufacturing System Engineering, School of Mechanical Engineering, Xi'an Jiaotong University, China.
** Corresponding author. State Key Laboratory for Manufacturing System Engineering, School of Mechanical Engineering, Xi'an Jiaotong University, China.
E-mail addresses: menlwang@xjtu.edu.cn (L. Wang), dcli@xjtu.edu.cn (D. Li).
[1] First author.

https://doi.org/10.1016/j.bioactmat.2024.12.033
Received 14 October 2024; Received in revised form 16 December 2024; Accepted 31 December 2024
Available online 8 January 2025

[5–9]. Microwire electrodes are among the earliest types of neural electrodes to be developed and successfully commercialized. Nowadays, microwire electrodes are commonly used to study neural activity in the brains of rodents, non-human primates, mammals, and humans, particularly in applications that require stable long-term performance or access to deeper brain structures [9]. These electrodes can be used to record the activity of single and multiple units, as well as to conduct long-term recordings of low-frequency brain signals. Research has demonstrated that microwire electrodes can continuously record neural signals from the guinea pig brain for up to 84 months, and other studies have shown the ability to achieve uninterrupted recordings of motor cortex signals in macaques for more than 9 months.

Currently, achieving long-term stable neural signal recording with implantable neural electrodes remains a grand challenge in BCI research. Numerous factors can affect the long-term performance stability of the electrodes, including the type of materials, the implantation methods used, and interface structure design. Poor biocompatibility of the electrodes often leads to a drastic decline in signal quality as the signal pathway is extended. Initially, signal detection rates are high, but as large proteins adsorb around the electrode and glial cells can encapsulate it, the recording sites become isolated from the neurons in both time and space, losing their ability to effectively record and modulate signals. Larger implantation trajectories can cause irreversible tissue and vascular damage, leading to inflammation and immune rejection reactions. Mechanical mismatch between the electrode and neural tissue during physiological activities like breathing and heartbeat can cause further penetration into the tissue, thus exacerbating damage to the recorded brain area. To expand the application range of implantable electrodes and to achieve stable high-throughput signal recording for a long period of time, improving the integration performance of the electrode-nerve interface has become the main development direction of implantable electrodes. Moreover, the technical barriers to achieving long-term stable recordings are now being addressed by exploring new design and functionalization strategies of different biomaterials to improve the flexibility of the electrode and the electrode-neural tissue interface [10].

The mismatches in mechanical strength between electrodes and brain tissue is a primary cause of brain damage. Therefore, the lower modulus of the neural electrodes possess, the lower damage they will potentially cause to brain tissue. Studies have shown that by means of using flexible electronic devices as implanted devices, chronic mechanical damage and immune responses can be significantly reduced, long-term recording of neural activity can be envisioned [11–13]. Currently, electrode flexibility can be achieved by using flexible materials as the substrate and wrapping rigid electrodes with flexible materials [14–20]. Chung et al. has fabricated a 1024-channel thin-film electrode with a total thickness of only 14 μm via integrating a modular polymer electrode array on a polyimide film substrate, which was able to record signals from hundreds of units across multiple brain regions in rats for over 160 days [10]. Beyond traditional materials, the use of new materials such as graphene-based transistors have attracted a great deal of attention to record brain activity. For instance, Masvidal-Codina and others developed a graphene-based flexible transistor array on a 10 μm thick polyimide flexible substrate, achieving high-resolution mapping of cortical activity at sub-low frequencies (<0.1Hz) [21–25]. Additionally, hydrogel materials used as coatings for electrodes offer a new approach to addressing mechanical mismatches between electrode-brain interface. Spencer et al. found that thick hydrogel coatings could reduce scar formation around electrodes 8week post-implantation [26–30]. By its turn, Tang et al. developed a new type of microfiber-shaped neural electrode, using carbon nanotube fibers and calcium-crosslinked sodium alginate as the core and sheath layers, respectively, with a low modulus (~10 kPa) [31] and excellent electrochemical performance was excellent and shown to be superior to most polymer-based flexible neural probes, however, the development of neural electrode flexibility is often accompanied by a sacrifice in its electrical performance.

To both reduce noise during signal recording and enhance the electrical and biological performance of electrodes, researchers have modified electrode surfaces with various materials, including those with special properties, biomolecules, and neuropharmaceuticals. In recent years, modifications using conductive polymers have become a mainstream technique for neural electrode enhancements. Conductive polymeric materials and hydrogels can offer several advantages over metal electrodes, such as drug encapsulation and release, binding with bioactive molecules or proteins, ionic exchange with tissues, and modulating cellular responses through changes in their physicochemical properties [32,33]. Common conductive polymers include poly(3, 4-ethylenedioxythiophene) (PEDOT), polypyrrole (PPy), polyaniline (PANI), and polythiophene (PT), which can be simply deposited on metal electrode surfaces through electropolymerization [34–37]. The thickness and thus the surface structure, biocompatibility, and electrical properties of such materials can be controlled by adjusting the polymerization parameters. For instance, Wang et al. deposited polyaniline nanoparticles on platinum (Pt) electrodes to form nanoscale structured films that facilitated electrical stimulation mimicking continuous neural impulses [38]. Di et al. studied polyaniline-modified Pt electrodes for stimulating and recording signals from mouse retinal neural tissue, finding that PANI modifications helped reduce inflammation and scar formation during long-term implantation [39]. To mitigate the inflammatory response in brain tissue following the implantation of neural electrodes, Wang et al. [40] developed CA/CS hydrogel coatings modified with anti-inflammatory drugs to reduce the initial inflammatory response after electrode implantation. However, the signal monitoring was conducted for 17 days only without long-term *in vivo* evaluation.

Therefore, it is crucial to establish a natural transition from mechanical, biological, to electrical aspects at the electrode-neural tissue interface for properly addressing primary failure issues of implanted neural electrodes. The development trends for electrodes are increasingly towards miniaturization, flexibility, and enhancing integration with the host tissue. However, these development trends also entail some compromises in other electrodes properties. Thus, balancing the physicochemical properties with biointegration capabilities is currently a major focus in electrode-engineering techniques. Therefore, designing and manufacturing novel implanted neural electrodes that avoid scar tissue formation is crucial for long-term, high-quality neural signal recording and transmission, and the application of neural electrode technology in biomedical and brain science fields.

In this study, we propose the design and performance evaluation of the bioaugmented electrode system for applications in BCI, the so-called bio-array electrodes. Considering the functional requirements and design criteria of bio-array electrodes, a numerical simulation model was developed to simulate the signal emission range within the neural tissues, and the optimal design of the neural electrode array was carried out. Bio-conductive coating materials were developed by preparing different composite conductive hydrogel formulations based on polyaniline-gelatin-arginine to produce coatings with heterogeneous gradient structures. The properties of the bio-array electrodes and hydrogel coatings were physicochemically characterized. The mechanical, rheological and electrochemical properties of the coatings were evaluated. Finally, the long-term *in vivo* performance of the bio-array electrodes was investigated using the C57 mouse model up to 60 days after implantation.

2. Materials and methods

2.1. Structural design

The design of a 16-channel biofilament array electrode, where the microfilament part of the electrode adopts a double helix winding structure, was performed. The electrode interface consisted of a 2 × 10 standard electrode interface. The connection between each channel's

microfilament and the electrode interface was achieved through a customized electrode substrate (Fig. 1A). Based on this neural microfilament array electrode, a design for a neural array electrode with a bio-enhanced coating structure is proposed. This design introduces a layer of bioconductive hydrogel material between the metal microfilament electrode and the brain tissue interface. Additionally, to ensure implant stability, an auxiliary sacrificial layer is coated at the base of the electrode array, which can provide temporary support during the implantation process while slowly dissolving.

2.2. Design optimization of array electrode site distribution

A simplified numerical model has been proposed simulating neural discharge in the brain cortex based on the natural neural firing and electrical signal transmission patterns of brain tissue. By means of employing the finite element method (FEM), the distribution of the electric field around neurons is calculated, subsequently the impact of different electrode arrangement designs on signal extraction efficiency is predicted, allowing for the optimization of the spatial distribution of electrode recording sites. Literature indicates that the density of cortical neurons in the human brain is approximately $1 \times 10^5/mm^3$, with neuron discharge rates typically concentrated around 5–10 Hz [41]. By simulating a static discharge state of neurons at a single instant, and setting each neuron to discharge at a frequency of 7Hz, approximately 1000 neurons are discharging simultaneously at any moment in 1 mm^3 of brain tissue. Further simplifying the model, a regular hexahedron was used to represent 1 mm^3 of brain tissue (Fig. 1B), assuming that the simultaneously discharging neurons are uniformly distributed within this hexahedral model, the distance between these neurons is estimated to be about 100 μm. While neural electrical signals can be efficiently transmitted through synaptic connections in neural networks, the transmission through neuron bodies and brain matrix encounters significant impedance due to the matrix's resistance. Simulation results show that the electric potential around neurons decays rapidly with distance, and when ignoring interactions between neurons, the potential distribution around a single neuron is depicted in Fig. 1C.

Other reports also suggest that the ambient noise in brain tissue is around 30 μV, and for electrode recording, the signal-to-noise ratio (SNR) of the neural signal to ambient noise needs to be greater than 2–2.5 [40]. Based on the analysis of the potential distribution of the static discharge model of neurons, it is indicated that the permissible distance from the neural electrode site to the neuron for detecting electrical signals is between 95 and 130 μm. Five different neural microfilament array electrode layouts were designed with inter-electrode distances of 50 μm, 100 μm, 150 μm, 200 μm, and 500 μm, respectively, arranged in a 4 × 4 matrix as shown in Fig. 1D-i. In a two-dimensional plane, calculations were made for the effective signal coverage area, the circumscribed coverage area, the overlapping collection area, the minimum and maximum number of cells collected, to evaluate the signal acquisition efficiency of different distance parameters (Fig. 1D). Table S2 summarizes the predicted signal collection efficiency of electrode arrays at different spacings, indicating that a 200 μm spacing is the most reasonable design. The array electrodes prepared subsequently in this study adopted this spacing setting.

2.3. Material properties evaluation

2.3.1. Microscopic morphology

The microstructure of coating materials was observed using a scanning electron microscope (SEM) to analyze the influence of different biocompatible material components on the size of the microscopic pores. Gel blocks measuring 5 × 5 × 2 mm^3 were prepared in prefabricated silicone molds. After the samples were cross-linked and cured, the surface moisture was absorbed using gauze and then placed in a freeze-dryer for 48 h. After freeze-drying, the samples underwent gold sputtering treatment. A field emission scanning electron microscope (SEM, SU-8010, Hitachi, Japan) was used to characterize the microstructure of the gel samples, observing pore size, particle aggregation levels, and other microstructural features. The pore sizes of the biomatrix materials under different material components and cross-linking conditions were measured using ImageJ software.

2.3.2. Mechanical properties test

The mechanical properties of coating material were evaluated to analyze the effect of different biocompatible material components on the compression modulus. Sample blocks were prepared in prefabricated silicone molds with size of 5 × 5 × 5 mm^3. After cross-linking in a calcium chloride solution, the samples were soaked in ultrapure water for 10 min and the surface was dried using blotting paper. A mechanical testing machine (ETM103A, Shenzhen Wance, with a 50N sensor) was used for the compression test, setting a loading speed of 2 mm/min and a travel distance of 2 mm. During the compression of the sample blocks, stress-strain curves were recorded.

2.3.3. Rheological properties test

The rheological properties were evaluated to investigate the effect of different biomaterial formulations on the final viscosity of the hydrogel-based coatings. A SNB-1 digital viscometer (Shanghai Fangrui, China) was used to perform constant temperature viscosity measurements on the biomaterials.

2.4. Fabrication of the bio-augmented neural microfilament array electrodes

2.4.1. Bioconductive coating materials preparation

The preparation process for the bioconductive coating material is shown in Fig. 2A. The prepared 5 wt% gelatin and 2 wt% sodium alginate gel solutions are preheated to 40 °C before mixed in a certain ratio until uniform in a clean bench, then 4 wt% polyaniline (PANI) powder is added and thoroughly dispersed to form an uncrosslinked conductive biogel. Subsequently, a sterile-filtered TG enzyme solution is added, and the mixture is stirred magnetically for 30 min. The uncrosslinked conductive biogel is then cooled down to 4 °C and soaked in a 1 % $CaCl_2$ solution in order to obtain the crosslinked bioconductive coating material.

2.4.2. Manufacturing of the bio-array electrodes

First, a single-core wire is wound into a double-helix core wire, which is then coated with the prepared bioconductive coating material before the entire electrode is encapsulated. A nickel-chromium alloy wire with a diameter of 30 μm and a Teflon insulation cover is wound into a 30 mm long helical conductive core with a pitch of 0.5 mm. Two beakers are filled with 10 mL of bioconductive coating material and 10 mL of $CaCl_2$ solution, respectively, and the ambient temperature is adjusted to ensure the fluidity of the bioconductive coating material. Using a three-axis motion platform to hold the electrode core wire, it is dipped about 3 mm deep into the bioconductive coating material, quickly immersed, and then placed into the $CaCl_2$ solution for cross-linking and curing for 5–10 s. This process is repeated 10 times until a uniform coating about 20 μm thick forms on the surface of the electrode wire. The coated electrode wire is then placed in a Petri dish sealed with a sealing film and pre-cooled in a −80 °C freezer for 4 h, followed by freeze-drying at a temperature gradient of −50 °C to −20 °C for 48 h to obtain a single-channel bioelectrode core wire covered with a bioconductive coating. Subsequently, array electrodes are prepared and encapsulated using standard procedures, including soldering the signal connection circuit board, positioning the ceramic perforated board, threading and positioning the electrode wire, applying polyethylene glycol for microfilament hardening, soldering the electrode wire to the circuit board, and finally encapsulating with AB glue. Additionally, array electrodes without the bioconductive coating are prepared as a control (Fig. 2C).

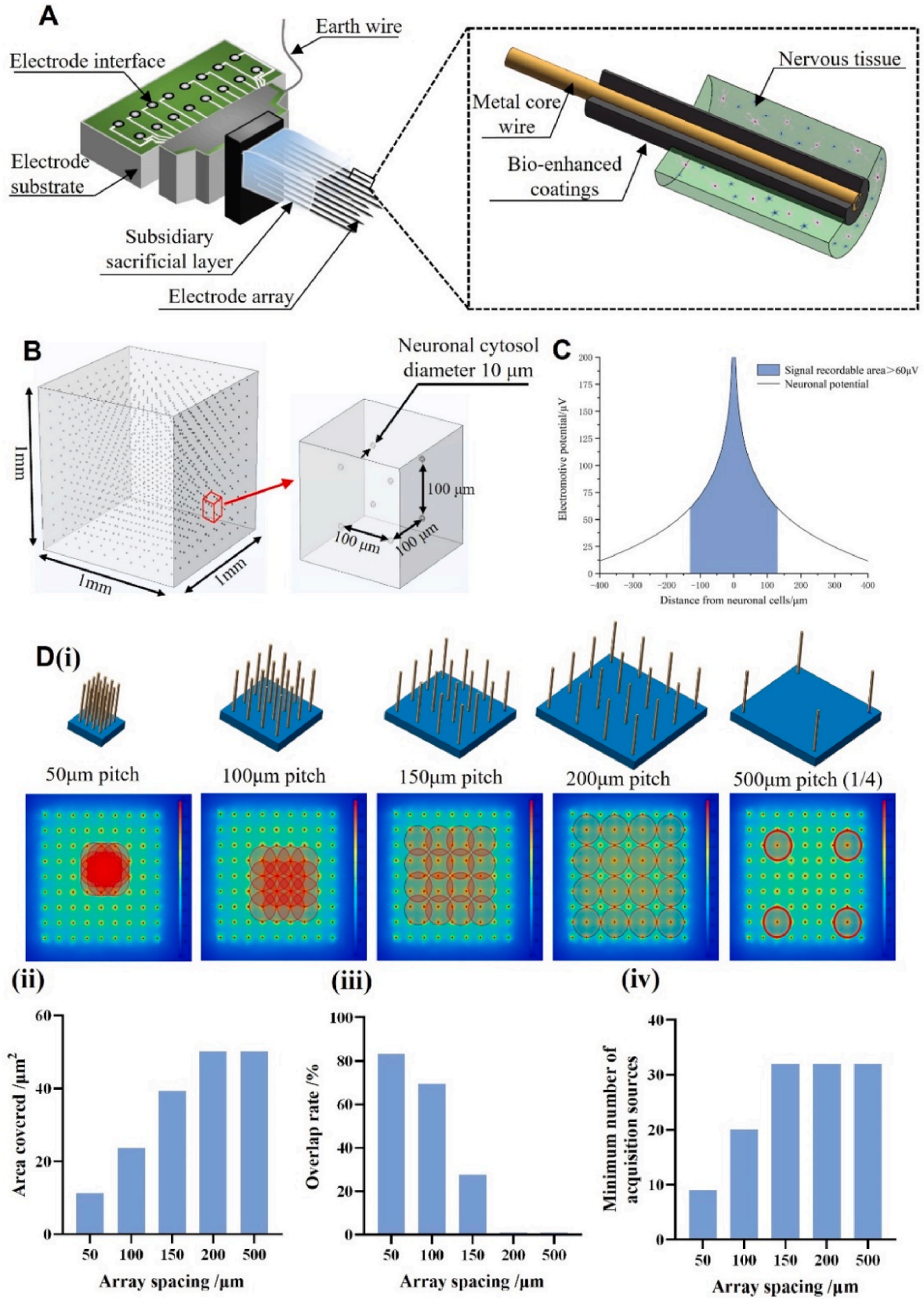

Fig. 1. Neural microfilament array electrode model structural design and site distribution optimization. A) Schematic design of bio-enhanced microfilament array electrode structure. B) Geometric model of neuronal static discharge (Model size of $1 \times 1 \times 1$ mm^3, neuron spacing of 100 μm, neuron firing frequency of 7Hz). C) Calculation of potential distribution at various distances from the neuron. D) i) Simulation of signal collection coverage for array electrodes at different spacings (red circles indicate the collection range of a single site within the array). ii) Receivable signal coverage area for different array spacing electrodes. iii) Overlap of receivable signal coverage for different array spacing electrodes. iv) Minimum number of acquisition sources for different array spacing electrodes.

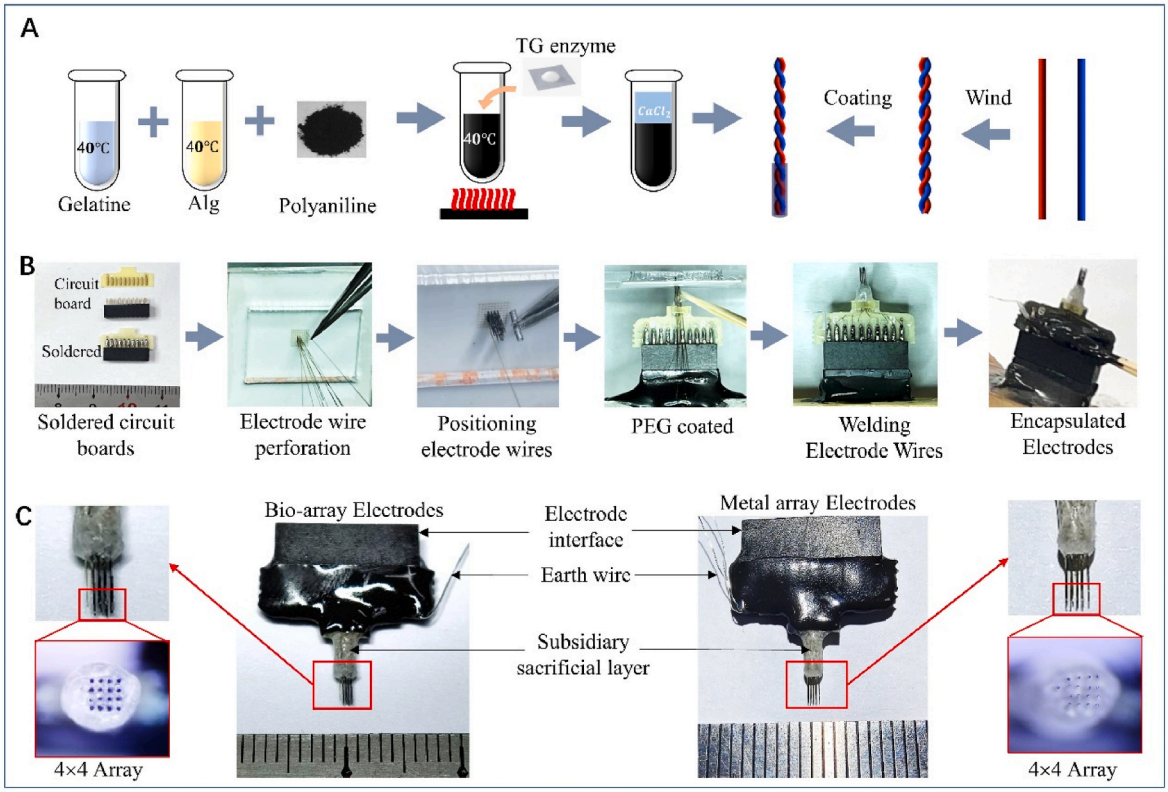

Fig. 2. Bio-array electrodes fabrication process. A) Preparation process for bioconductive coating materials and fabrication process for biologically enhanced microfilaments. B) Encapsulation process for biologically enhanced array electrodes. C) Finished array electrodes (Bio-array electrodes: bioaugmented array of implantable electrodes; Metal array electrodes: metal array of implantable electrodes).

2.5. Electrochemical performance evaluation

Electrochemical testing of the prepared electrodes was conducted using a Princeton v3 electrochemical workstation, establishing a three-electrode system with a platinum sheet electrode and a silver electrode serving as the counter electrode and reference electrode, respectively. Electrochemical performance of the array electrodes was evaluated using methods including cyclic voltammetry, electrochemical impedance spectroscopy, and constant current charge-discharge techniques.

2.5.1. Evaluation of electrode surface charge

Cyclic voltammetry tests (Princeton versa3F, USA) were conducted on both biological and metal array electrodes (n = 4) using a three-electrode system. The scan voltage range was set from −0.7 to 0.7V, with a scan rate of 500 mV/s. The relative changes in current and potential were recorded to obtain cyclic voltammetry curves. The cyclic voltammetry curves typically appear closed, and the charge transfer Q on the electrode surface can be calculated based on the enclosed area S of the curve using Eq. (1).

$$Q = \frac{S}{2v} \quad \text{(Eq.1)}$$

where: Q——charge throughput/C; S——closed area of cyclic voltammetry curve/V•A; v——scanning speed/V/s.

2.5.2. Electrode impedance test

Electrochemical impedance analysis (Princeton versa3F, USA) was performed on both biological and metal array electrodes (n = 4). Similar to the setup for single-channel neural electrodes, the output disturbance amplitude was set at 50 mV, with a frequency range from 0.1Hz up to 1×10^6 Hz. The resulting electrochemical impedance spectra for both electrodes were obtained.

2.5.3. Electrode capacitance test

The charge-discharge performance of biological and metal array electrodes (n = 4) was studied by setting the voltage range from −0.7V to 0.7V and a constant current of 0.05 μA. The resulting constant current charge-discharge curves for the array electrodes were obtained. By analyzing the relationship between potential and time, the charge-discharge performance and specific capacitance C of the electrodes can be studied. The specific capacitance C is calculated according to Eq. (2):

$$C = \frac{I \bullet T}{Eh\text{-}El} \quad \text{(Eq.2)}$$

where: Eh——max. voltage/V; El——min. voltage; I——a set constant current/A; T——constant current charging and discharging cycle/s.

2.6. In vivo brain tissue damage study

2.6.1. Animal test

C57 mice were selected for long-term neural signal acquisition and evaluation of the long-term biocompatibility of neural electrodes. Two groups of animal model, with five mice in each group, were established, in which the bio-array electrodes and metal array electrodes were implanted, respectively. A stereotaxic instrument (ZhongShi, China) was employed to navigate the electrode array into the prefrontal cortex of the mouse brain at a depth of 2 mm, 1.75 mm anterior and 0.3 mm lateral to the bregma. First, the mouse was anesthetized with isoflurane inhalation anesthesia, and the skull was exposed after the fur shaving, then the mouse was secured onto the stereotaxic instrument. Incision was made on the scalp and mucosa to expose the pre-drilled position on the skull, then the electrode implantation site was accurately located

and marked via the stereotaxic instrument. Three holes of approximately 0.6–1 mm deep were drilled outside the implantation area and screws were inserted. One hole of approximately 2 mm diameter was drilled in at the electrode implantation site to expose the dura mater. A needle was used to pierce the dura mater and add brain buffer solution into the exposure to maintain a normal brain tissue environment. After being connected to the signal acquisition system, the electrode array was implanted slowly into the cortex via the Z-axis arm of the stereotaxic instrument, advancing 200 μm every 5 min until the implantation depth reaches 2 mm. Then the electrode was fixed with bone cement (Homtopy, USA) to finish the implantation process. Afterwards, brain electrical signals can be collected immediately as acute electrophysiological data, or for long-term *in vivo* brain electrical signal collection.

2.6.2. Signal acquisition and analysis

Electrophysiological signals from electrodes were collected using a neural electrode electrophysiological signal acquisition system (Zeus 128-channel system, Nanjing Bio-signal, China), which allows for high-precision surgical implantation of electrodes in small animals and comprehensive monitoring of acute/chronic signals across 128 channels. The array electrodes were implanted 1.75 mm anterior and 0.3 mm to the left of the frontal cortex, at a depth of 2 mm, in the brains of mice. Real-time brain electrical signals recorded by the electrodes were collected from the moment the implantation depth reaches 1 mm until the end of implantation (approximately 30 min), serving as acute electrophysiological signals. During the collection of action potential signals, the filtering range was set between 500 and 7500Hz with a sampling rate of 30K/s, and signals with a signal-to-noise ratio (SNR) greater than 2.0 were selected. For local field potential (LFP) signals, the sampling rate was set at 2K/s with a filtering range of 0.3–300Hz. The collected signals were stored on a computer for further analysis. The LFP signals were analyzed using NeuroExplorer (Plexon, USA) to conduct spectral analysis, calculate the power spectral density, and to identify different rhythmic distributions in the LFP signals from the waveform data. The action potential signals are analyzed using Offline Sorter software (Plexon, USA), commonly used for processing and analyzing action potential signals.

2.6.3. The brain tissue damage analysis

Animals with implanted electrodes were sacrificed at predetermined time points for brain damage study, and four animals from each control group ($n = 4$) were selected for long-term *in vivo* biocompatibility test of the electrodes. After anesthetization, cardiac perfusion was performed using 150 ml of 0.9 % NaCl solution containing heparin, followed by the extraction of brain tissue, which was then fixed in 4 % paraformaldehyde solution at 4 °C for 24 h. Tissue blocks surrounding the electrode were extracted along the axis parallel to the electrode at size of 3×3 mm^2 using a mold, and then paraffin-embedded. Horizontal cryosections (20 μm thick) were made starting 0.5 mm below the cortical surface (perpendicular to the electrode axis). Every fifth section was collected on poly-lysine-coated slides, with ten sections per sample selected for observation. A vertical microscope was used to analyze the overall morphology of damage in the brain sections. A confocal laser microscope was used to analyze the depth of damage at the electrode implantation sites in the tissue, images of brain tissue defects were captured and the depth of damage were measured. After Hematoxylin and Eosin (HE) staining, tissue reactions and glial encapsulation were evaluated. ImageJ software was used for quantitative analysis of the stained images, including cell count, cell aggregation thickness, tissue defect area, and fluorescence intensity distribution. Origin software was used to plot graphs of fluorescence intensity versus location, and analyze the relationship between cell aggregation and electrode positioning.

2.7. Statistical analysis

In this study, the experimental data were analyzed for significance using a three-factor analysis of variance (ANOVA) method and Tukey's multiple comparisons test, where a p-value of less than 0.05 was considered statistically significant (*$p < 0.05$, **$p < 0.01$, ***$p < 0.001$).

3. Results

3.1. The properties of composite polyaniline-gelatin-alginate based conductive hydrogels

To investigate the effect of gelatin/sodium alginate content on the rheological properties of biomaterials, the viscosity of the biomaterials with different components was measured. In Fig. 3A, a positive correlation was observed between viscosity and concentrations of gelatin and sodium alginate was observed, peaking at 650.25 ± 27.9 mPa•S when 7 wt% of gelatin and 4 wt% of sodium alginate were used. Notably, sodium alginate exerted a significant influence on material viscosity. Additionally, to examine the influence of gelatin/sodium alginate content on the modulus of the biomaterials, the compressive modulus of the biomaterials with different compositions was tested. The results (Fig. 3B) showed that the compressive modulus increased along with the concentrations of gelatin and sodium alginate, achieving a maximum of 55.2 ± 3.1 kPa at the same concentrations (gelatin 7 wt%/sodium alginate 4 wt%), with sodium alginate playing a major role in affecting the compressive modulus of the materials. To minimize the mechanical mismatch between the neuro-electrode and the brain tissue, a material combination with the lowest possible modulus should be selected. Additionally, selecting a material combination with moderate viscosity is crucial for the coating process. Based on the analysis results, a biomatrix material consisting of 5 % gelatin and 2 % sodium alginate was initially chosen. The microstructure, mechanical properties, and conductivity of bioconductive hydrogel samples were investigated in this study at different polyaniline concentrations (Fig. 3). The results indicate a gradual decrease in the micro pore size of the biomaterials with increasing polyaniline concentration, ranging from 101 ± 14 μm to 61 ± 10.6 μm. Polyaniline particles are uniformly distributed within the porous structure, and as the polyaniline concentration increases, the surface roughness of the micropores also increases. The pore sizes were statistically analyzed using ImageJ software, as shown in Fig. 3D. The mechanical properties of the material system at different polyaniline concentrations are depicted in Fig. 3E. The electrochemical properties of the biomaterial at different polyaniline concentrations are shown in Fig. 3F.

3.2. Evaluation of electrochemical performance of bio-augmented array neural electrodes

The electrochemical performance of the bio-array electrode and the metal array electrode was evaluated using an electrochemical experimental testing system in this study. The specific parameters are shown in Table S.3, and the results are presented in Fig. 4. Cyclic voltammetry was performed on both the bio-array electrodes and the metal array electrodes, and the cyclic voltammograms are illustrated in Fig. 4B. The results indicate that the closed area of the cyclic voltammogram for the bio-array electrodes is significantly larger than that of the metal array electrodes. Further statistical analysis of the current variation range and the area under the cyclic voltammogram for both types of array electrodes was conducted, and the charge transfer quantity Q was calculated using Eq. (1). It was found that the bioaugmented array electrodes (substitute bio-array electrodes in the following text) exhibited a higher conduction current value (−1.21 to 1.92 μA) and a greater surface charge transfer quantity (14.11 ± 0.36 × 10^{-7}C). This is an indication that the bioconductive gel coating significantly improved the conductivity of the array neural electrodes (with a 1.74-fold increase in charge transfer), and the array electrodes prepared in this study exhibited good consistency among the different electrode sites. To verify the

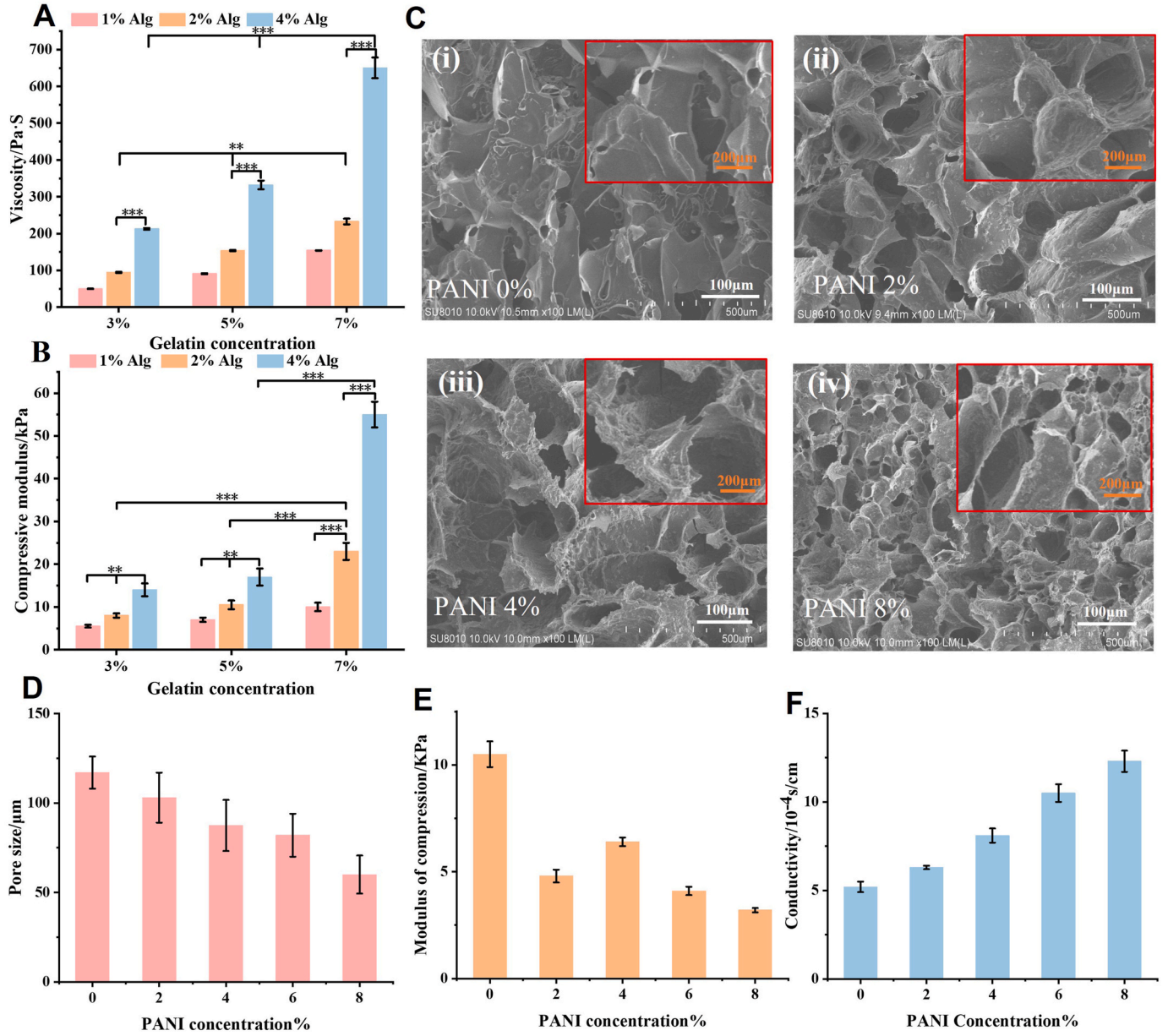

Fig. 3. Optimization of conductive composite Polyaniline-Gelatin-Alginate based conductive hydrogel material. A) Viscosity of hydrogels with different material formulations, in particular using Alginate at concentration of 1 wt%, 2 wt% and 4 wt%, gelatin at concentration of 3 wt%, 5 wt%, and 7 wt%. B) Compressive modulus of hydrogels with different material formulations. C) Scanning electron microscopy images of hydrogels comprising PANI at different concentrations (0 wt %, 2 wt%, 4 wt%, and 8 wt%). D) Pore size of hydrogels at different PANI concentrations. E) Compressive modulus of hydrogels comprising PANI concentrations: i) 0 wt%, ii) 2 wt%, iii) 4 wt%, and iv)8 wt%. F) Conductivity of hydrogels at different PANI concentrations. (Alg: sodium alginate; PANI: polyaniline); (n = 3; error bars represent standard deviation; three-factor analysis of variance ANOVA; Tukey's multiple comparisons test, *p < 0.05, **p < 0.01, ***p < 0.001).

electrochemical stability of the bio-array electrodes, a comparison was made before and after conducting 1000 cycles of cyclic voltammetry testing. The results (Fig. 4C) indicate the excellent electrochemical stability and durability of the bio-array electrodes in PBS. The closed-loop voltammograms of each channel (n = 16) of the bio-array electrode and the metal array electrode were measured and the area under the curves was calculated for each channel to obtain the charge throughput according to Eq. (1). The results of the charge throughput for each channel of the bio-array electrode and the metal array electrode are shown in Fig. 4D. The results indicate that the fluctuation range of the charge throughput in each channel of the bio-array electrodes is larger than that of the metal array electrodes, which may be caused by manufacturing variations between individual microfilaments resulting from the bioconductive coating applied to the bio-array electrodes. Electrochemical impedance analysis was performed on both types of electrodes, and the electrochemical impedance spectra of the two array electrodes are shown in Fig. 4E. The results indicate that at the neuronal extracellular signal frequency of 1 kHz, the average impedance of each channel of the metal array electrodes is 3769Ω, while the average impedance of each channel of the bio-array electrodes is reduced by 63.17 % compared to the metal array electrodes. This suggests that the bioconductive coating can significantly reduce the impedance of the array electrode and improve its recording and stimulation ability. The results also indicate that the previously optimized layout array structure did not affect the impedance of the bio-electrodes. The impedance of each channel of both types of electrodes was statistically analyzed around 1Hz as shown in Fig. 4F. This demonstrates that the fluctuation range of impedance for bio-array electrodes is 4.8 %, which is much

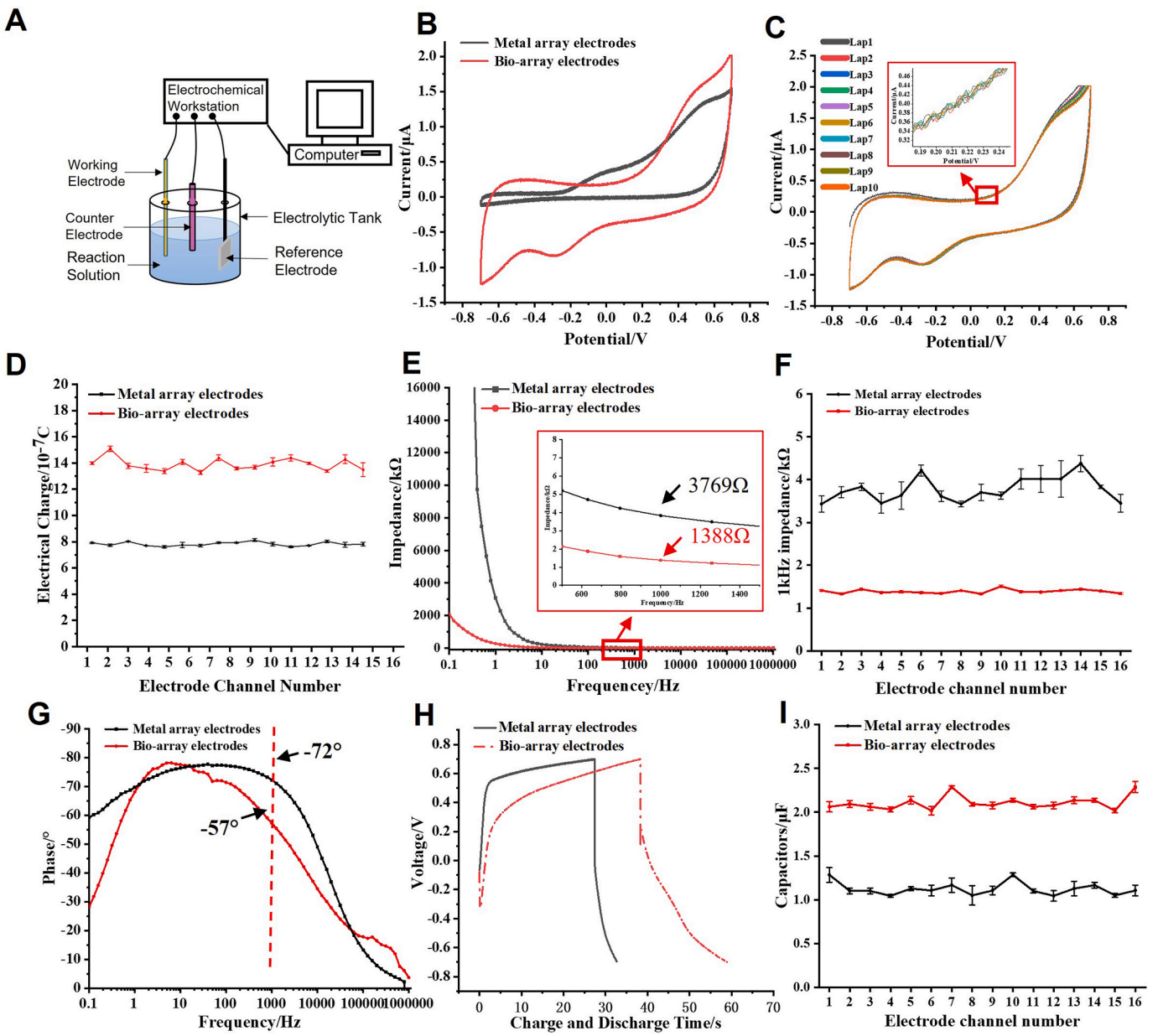

Fig. 4. Electrochemical performance of both the bioaugmented and metal array electrodes. A) Schematics of the three-electrode testing system (Counter electrode: Pt; Reference Electrode: Ag). B) Voltammetry curves (Scanning voltage of −0.7~0.7V, scanning speed of 500 mV/s). C) Cyclic voltammetry curves at a scanning rate of 500 mV/s for 10 cycles (Scanning voltage of −0.7~0.7V, scanning speed of 500 mV/s). D) Charge passing through each channel. E) Impedance-frequency relationship (Peak impedance of 50 mV, frequency range of 0.1Hz–1 × 10^6 Hz). F) Impedance values of each channel at a scan frequency of 1 kHz. G) Phase-frequency relationship. H) Charge-discharge curve under constant current density of 0.05 μA (Voltage range of −0.7V–0.7V, constant current setting of 0.05 μA). I) Current values in each channel under constant current density of 0.05 μA (Bio-array electrodes: bioaugmented array of implantable electrodes; Metal array electrodes: metal array of implantable electrodes). (n = 3; error bars represent standard deviation).

smaller than that of metal electrodes, suggesting higher impedance stability for the bio-array electrodes. The relationship between the impedance of the array electrodes and the signal frequency was analyzed to obtain information about the electrochemical reaction processes, as shown in Fig. 4G. The results demonstrate that at around 1 kHz, the phase angle for the metal array electrodes is −72°, while it is −57° for the bio-array electrodes, indicating improved Faradaic charge conduction capability exhibited by modified array electrodes and highlighting enhanced electrical conductivity performance of bio-conductive coatings on array electrodes. The constant current charge-discharge curves obtained during the charging and discharging process of the two types of electrodes are shown in Fig. 4H. It can be seen that the charge-discharge curves of the two array electrodes are similar, but the charge-discharge cycle of the bio-array electrode is significantly prolonged, indicating a significant increase in capacitance after coating with a bioconductive coating. The capacitance values for each channel of the bioarray electrode and metal array electrode were statistically analyzed (Fig. 4I). The results show that the impedance fluctuation range for each channel of the bio-array electrode is 12.5 %, which is slightly larger than that of the metal array electrodes but still within an acceptable range.

3.3. *In vivo electrophysiological evaluation*

Based on animal experiments, the acute recording capability of the bio-array electrodes for LFP signals were tested using a three-electrode

testing system (Fig. 5A). A bio-array electrodes (200 μm) was used to record the LFP signals from the mouse prefrontal cortex, with a signal sampling rate of 2K/s and a filtering range of 0.3–300Hz. The experimental results of the field potential signals from the biological electrodes are shown in Fig. 5B. The bio-array electrodes can clearly record the LFP signals of the mouse cortex in all 16 channels, and the distribution of signal rhythms (Fig. 5C) conforms to the characteristics of LFP signals in anesthetized mice. The total number of neurons recorded during electrode implantation and after implantation was compared between bio-array electrodes and metal array electrodes (Fig. 5D). The results showed that the total number of neurons recorded by bio-array electrodes was 1.6 times that of metal electrodes, with an average of more than 2 action potential signals recorded per channel. The extracted and analyzed action potentials recorded by each channel of the two array electrodes are shown in Fig. 5E.

3.4. Long-term In vivo electrophysiological evaluation

Long-term monitoring of neural electrical signals in mice implanted with neural electrodes was conducted, and the results at 10, 20, 30, 40, 50, and 60 days were analyzed as shown in Fig. 6. When comparing the peak firing rates recorded from the bio-array electrodes and metal array electrodes post-implantation, it was found that the bio-array electrodes detected a higher number of neuronal firing signals on average (Fig. 6B), thus indicating a lower acute rejection response of neurons towards the bio-array electrodes. The average signal-to-noise ratio (SNR) of field potentials for bio-array electrodes and metal array electrodes at different time points (Fig. 6C) and the specific values of field potential SNR values for each channel (Fig. S1B) were statistically calculated. Although significant fluctuations can be observed in local field potential SNR among different channels for bio-array electrodes, overall, the bio-array electrodes outperformed the metal array electrodes. As the implantation time of the electrodes increased, the SNR of the LFPs from the bio-array electrodes decreased from 6.2 and stabilized around 4.2. In contrast, for the metal array electrodes, the SNR began to decrease from 4.2 to 3.3 starting from day 20, and this downward trend continued, indicating that the noise in the signals recorded by the metal electrodes gradually increased over time. Principal component analysis was performed on the unit potentials (peaks) implanted at different time points, as shown in Fig. 6D. The closed circle represents the center, and the ellipse represents the contour of two standard deviations (2σ) of the principal component distribution. The clusters corresponding to individual units of neural signals recorded by the bio-array electrodes at different time points show significant overlap, whereas the metal array electrodes were only able to detect neural signals at 10 and 30 days. This indicates that, compared to metal array electrodes, bio-array electrodes possess the capability for continuous recording of single neuron signals. Further statistical analysis of the SNR for different channels at different times was conducted, and the results are shown in Fig. 6E. The SNR of the bio-array electrodes is 2.1 times of the metal electrodes. The number of neurons detected over a long-term period was statistically analyzed (Fig. 6F and Fig. S1), revealing that both types of electrodes gradually recorded an increasing number of neurons in the first 30 days after implantation. Subsequently, the number of neurons recorded by both types of electrodes decreased, but the bio-array electrodes detected significantly more neural signals than the metal electrode. This result suggests that after 30 days of implantation, the metal electrode may be more severely affected by encapsulation with scar tissue (Fig. 7A and B), leading to a sharp decline in signal recording capability, whereas the bio-electrode demonstrates excellent electrophysiological recording ability in comparison.

3.5. Evaluation and analysis of electrode-Induced brain tissue damage

The brain tissue damage at the electrode implantation site and the inner cranial electrode extraction site were observed using a vertical microscope, as shown in Fig. 7A–i,ii and 7B-i,ii. It can be seen that after the bioelectrodes were pull out from the brain, both surfaces of the

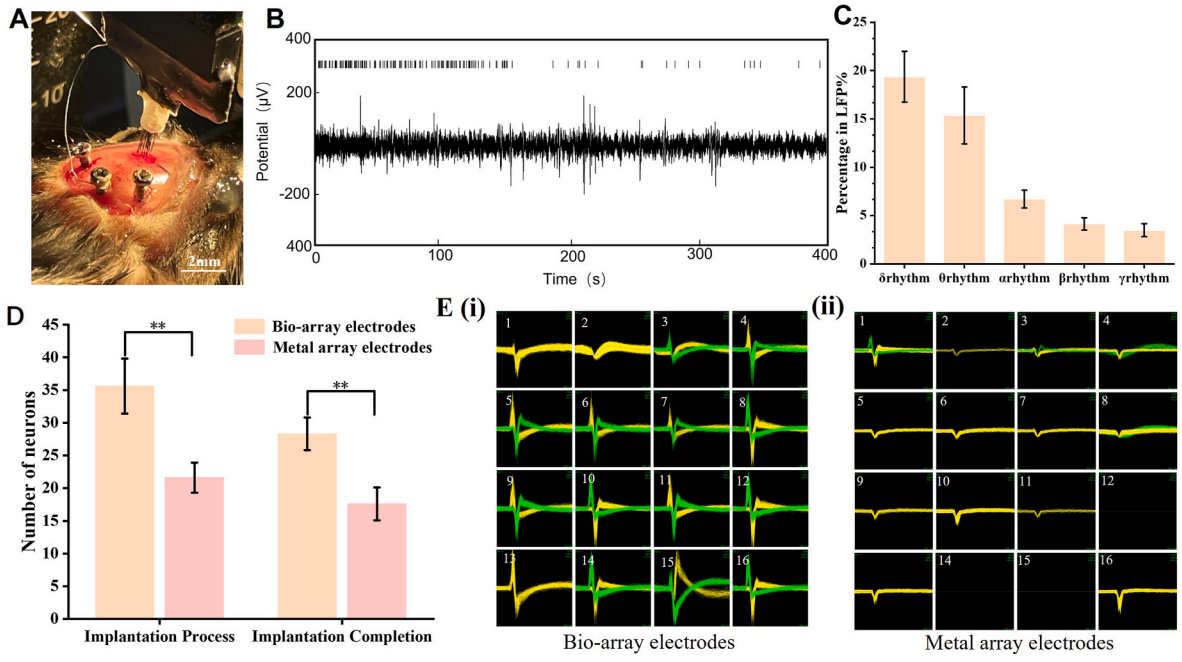

Fig. 5. Evaluation of the *in vivo* electrophysiological performance of the electrodes. A) Photograph of the bio-augmented neural microfilament array electrode implanted in brain of mice. B) Single-channel recording of LFP spectrogram using bio-array electrodes (Signal sampling rate of 2K/s, filter range 0.3–300Hz). C) Different rhythmic distributions of LFP signals recorded by bio-array electrodes. D) Comparison of the number of acute neuronal recordings between bio-array and metal array electrodes (Filter range of 500–7500Hz, sampling rate of 30K/s). E) Recording conditions for spike signals in different channels: i) with bio-array, and ii) metal array electrodes. (Bio-array electrodes: bioaugmented array of implantable electrodes; Metal array electrodes: metal array of implantable electrodes). (n = 3; error bars represent standard deviation; Tukey's multiple comparisons test, *p < 0.05, **p < 0.01, ***p < 0.001).

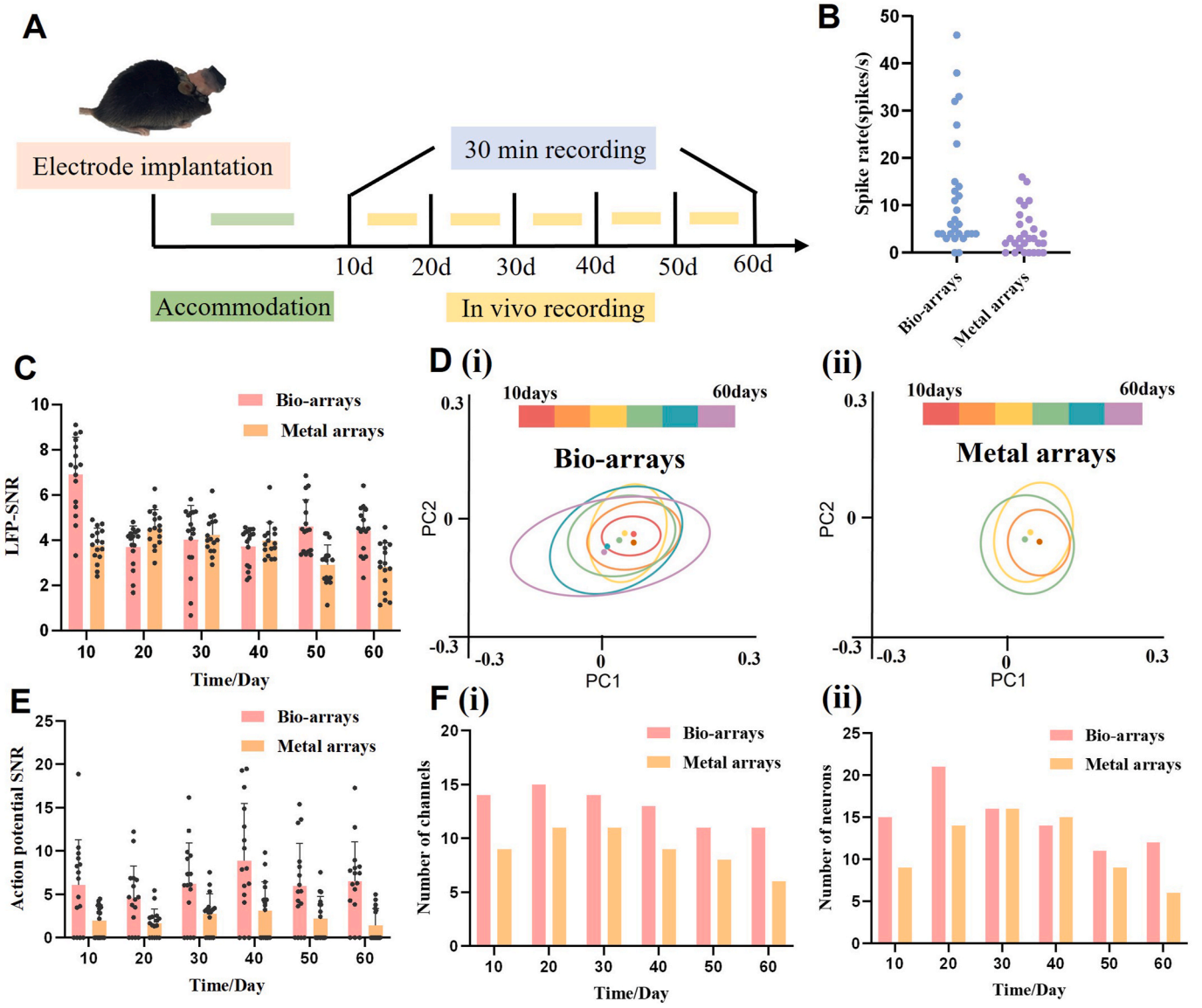

Fig. 6. Long-term evaluation of the *in vivo* electrophysiological performance of the electrodes (Acquisition frequency of 30 kHz, bandpass filtering frequency range of 500~7500Hz). A) Schematic diagram of long-term signal recording from neural electrodes. B) Comparison of spike rates between bio-array electrodes and metal array electrodes. C) Average SNR of LFP signals at different time points for both array electrodes. D) Principal component analysis of unit potentials (spikes) recorded from both array electrodes over 10–60 days post-implantation: i) bio-array electrodes, and ii) metal array electrodes. (Closed circles represent the centers, and ellipses indicate the two standard deviation (2σ) contours of the principal component distribution). E) Average SNR of action potentials at different time points for both array electrodes. F) Number of channels and neurons capable of recording spike signals at different times: i) and number of spike signals that can be recorded over time. ii) for both electrodes. (Bio-arrays: bioaugmented array of implantable electrodes; Metal arrays: metal array of implantable electrodes). (n = 16; error bars represent standard deviation).

cortical and the electrode remain smooth, and a certain amount of bioconductive coating material remained at the implantation site. However, after the removal of metal electrodes from the brain, a large amount of brain tissue was found to be surrounded with the electrode, left apparent damage to the cortical surface. After immunofluorescent staining, the slices from each group were observed under a laser confocal microscope, as shown in Fig. 7A and B. In Fig. 7A-iii, only a small number of astrocytes were found to be clustered around the bio-array electrode, while there was almost no astrocyte aggregation around the outer ring electrodes. The neurons were evenly distributed without any signs of neuronal degeneration. Additionally, no small glial cell clusters were detected around the bio-array electrodes in Fig. 7A-iv. As for Fig. 7B-iii, due to the extraction process of the metal array electrode which brought out a large amount of brain tissue, only residual tissue cavities could be observed with jagged inner walls and severe tissue damage. Numerous star-shaped glial cells were found to be clustered around these cavities with abundant stained cell nuclei nearby but sparser distribution of neurons near the electrodes and signs of neuronal degeneration appeared. From Fig. 7B-iv, a large number of small glial cells were found to be aggregated around the metal array electrode.

ImageJ image analysis software was used to process the stained result images and quantitatively analyze the aggregation of glial scars around different channel electrodes, as shown in Fig. 7C. By statistically calculating the relationship between GFAP fluorescence intensity and the distance away from the electrode for each channel, it is possible to analyze the aggregation of astrocytes at different electrode channels. Few star-shaped glial cells were found to aggregate in the vicinity of biological electrodes, with cell density returning to normal tissue levels at a distance of approximately 50 μm from the electrode; whereas around metal electrodes, there was a significant expansion in the range

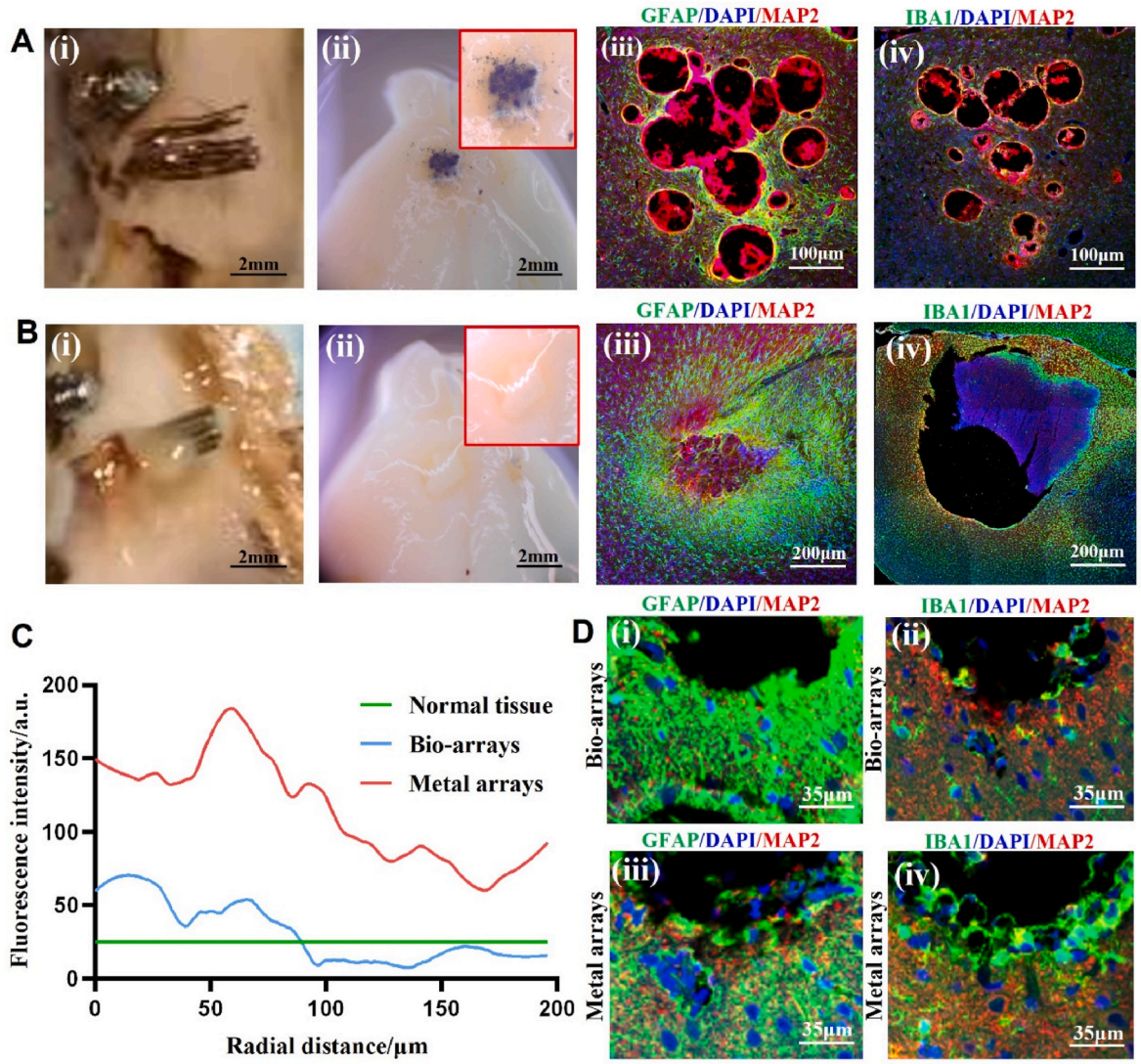

Fig. 7. The histological studies of the brain tissue around two types of electrodes after 12 weeks of implantation. A) Photographs of the bio-array electrodes. i) Images of the electrodes after removal. ii) Images of the brain tissue around the electrodes. iii) The immunofluorescence histological staining of astrocytes and neurons around the electrodes. iv) The immunofluorescence histological staining of microglia and neurons around the electrodes. B) Photographs of the metal array electrodes: i) Images of the electrodes after removal. ii) Images of the brain tissue around the electrodes. iii) The immunofluorescence histological staining of astrocytes and neurons around the electrodes. iv) The immunofluorescence histological staining of microglia and neurons around the electrodes. C) Statistical comparison of immunofluorescence intensity between the two types of electrodes. D) Immunofluorescence histological evaluation of morphological changes of astrocytes and microglia in the surrounding tissue of the two electrodes (GFAP:green, DAPI:blue, MAP 2:red, and IBA 1:green). (Bio-arrays: bioaugmented array of implantable electrodes; Metal arrays: metal array of implantable electrodes).

of glial cell aggregation (greater than a distance of 400 μm).

4. Discussion

In response to the demands for improved bio-adaptation between implanted neural electrodes and brain tissue, this study proposes a novel design concept for neural electrodes featuring a bio-enhanced coating structure. By integrating numerical simulation with experimental approaches, the structure, materials, and performance of each component of the electrode were optimized. The bio-enhanced design's effects on the long-term *in vivo* biocompatibility and electrical signal acquisition capability of the electrode were validated through both *in vitro* and *in vivo* experiments.

A bio-conductive material for neural electrode surface coatings has been developed in this study, and the physical, electrochemical, and biological properties were analyzed systematically. By evaluating the properties of the bio-conductive materials with different compositions, the optimal composition suitable for neural electrode coating was identified. The microstructure, mechanical properties, and conductivity of bioconductive hydrogel were systematically investigated in this study at different polyaniline concentrations, indicating that the micro pore size of the hydrogel would increase along with the concentration of polyaniline, so does the surface roughness. However, the compressive modulus of the conductive biomaterials was found to decrease with the addition of polyaniline. At a polyaniline (PANI) concentration of 8 wt%, there is a reduction in compressive modulus by 70 %. Although this value exceeds the range found in natural brain tissue (0.5–1 kPa), it remains considerably lower than that observed for metal electrodes. Such reduction in modulus aids in minimizing damage to surrounding brain tissue; however, it may pose challenges during electrode design and preparation to strike a balance between biocompatibility and mechanical performance. The electrochemical properties study indicated that the conductivity of the hydrogel materials increases proportionally with the increasing concentration of polyaniline; specifically, reaching a

conductivity value that is 2.8 times higher than that of the pure hydrogel material when the polyaniline concentration is 8 wt%. The increase in conductivity exhibits a nearly linear trend, with bioconductive materials exhibiting conductivities ranging from 10^{-4} to 10^{-3} S/cm. Ieva et al. found that hydrogel scaffolds with pore sizes around 100 μm were more suitable for neuronal regeneration in their study [42], and to satisfy the low modulus with high conductivity and to facilitate neuronal growth, the concentration of added polyaniline was subsequently chosen to be 4 wt% in this study.

In this study, a systematic and comprehensive evaluation of the electrochemical performance was conducted for the fabricated bio-enhanced array electrodes and the comparative metal electrodes. The results of cyclic voltammetry tests demonstrated that, compared with metal array electrodes, the bio-enhanced array electrodes exhibited a significantly increased cyclic voltammogram area, with the charge transfer capacity improved by 1.74 times. Comparison of results from multiple cycles revealed that the charge transfer fluctuation across channels of the bio-enhanced array electrodes was only 13.3 %. Electrochemical impedance spectroscopy analysis showed that after modification with the bio-conductive coating material, the impedance of the array electrodes at approximately 1 kHz decreased by 63.17 %, demonstrating enhanced Faradaic charge transfer capability. Additionally, the impedance fluctuation across channels of the bio-enhanced array electrodes was only 4.8 %. Constant current charge-discharge tests revealed that the average capacitance of the electrodes increased from 1.14 μF to 2.11 μF after modification with the bio-conductive material. Electrochemical test results indicated that the designed and fabricated array electrodes did not compromise the signal recording capability of individual electrodes despite the increased number of electrode channels. The bio-enhanced neural array electrodes demonstrated excellent electrochemical performance and stability.

This is due to the uneven surface morphology caused by the coating process. The hydrogel coating on the electrode surface is characterized by a vast network of pore structures that create numerous efficient electron/ion transport channels. This design results in a higher specific surface area and charge injection capacity (CIC), thereby enhancing electrolyte penetration into the electrode material. Consequently, this leads to increased charge storage capacity (CSC) [43] and reduced impedance, significantly boosting the electrochemical performance of the electrode material [44] and improving the SNR [45]. However, the porous structure also induces pore resistance, which limits the depth of penetration into the pores as the signal frequency increases [46]. This pore resistance grows with frequency, allowing the electrodes to maintain stable impedance even under high-frequency signals. This results in a lower standard deviation of measured signals and reduced measurement uncertainty, making them particularly advantageous for action potential recording [47].

In order to evaluate the long-term biological integration performance of neural electrodes within brain tissue *in vivo*, animal experiments were conducted. Immunohistochemistry was performed on brain tissue slices to examine the distribution and encapsulation of glial cells surrounding the electrodes at different implantation durations. This study provides new insights into the electrodes' biocompatibility, signal acquisition capabilities, and related performance metrics. The results indicate that the bio-array electrodes can clearly record LFP signals in mouse cortex and can capture multiple neuronal firings. The waveform of the signal conforms to the characteristics of anesthetized mouse LFP signals, demonstrating that the prepared multi-channel bio-array electrodes have good acute capability for collecting LFP signals. Compared with metal array electrodes, bio-array electrodes can simultaneously record neuronal discharge signals with greater peak amplitudes and larger quantities. This indicates that the multi-channel bio-array electrodes prepared in this study has excellent electrophysiological recording capability, with each channel able to record clear action potential signals and exhibiting strong stability in performance. Both types of electrodes exhibited a decreasing trend followed by an increasing trend, and then another decrease as recording time increased. This may be due to a significant increase in immune rejection reactions from brain tissue with longer implantation time, reaching its peak at around 20 days, resulting in a high concentration of glial cells surrounding the electrode and decreased neuronal activity leading to reduced SNR. However, as the implantation time continued, the immune response alleviated, causing a recovery in SNR. Nevertheless, with further increase in implantation time, glial scar formation occurred around the metal array electrodes while glial cell density decreased around the bio-array electrodes, resulting in a sustained decrease in SNR for metal array electrodes but stable high SNR for biological electrodes detecting neural action potentials. Chan et al. [48] developed a highly flexible silicon-based microelectrode array through a modification of the recording sites with PEDOT:PSS/pHEMA conductive hydrogel, which could effectively enhance the signal detection resolution by 200 %, comparable to the results obtained in this study. However, the modification was limited to the recording sites and did not address the issue of biointegration caused by the mechanical mismatch between the overall neural electrode and brain tissue. Additionally, only 3 weeks of *in vivo* study was conducted in their study. Fallon et al. [49] employed a PVA/PEDOT composite material to modify neural Pt electrodes, significantly enhancing their charge injection capacity and reducing impedance, thereby improving the SNR of the electrodes. However, the electrodes fabricated in their study had a diameter of 300 μm, which is substantially larger compared to those developed in this study (80 μm).

Implantation experiments demonstrated that the bioaugmented layer on the electrode surface played a beneficial role in disguising as well as reducing mechanical damage to brain tissue during both the electrode implantation process and long-term implantation, therefore, causing minimal damage to the brain tissue compared to the metal electrodes.

The immunohistochemical staining results of the brain tissue around two electrodes after long term implantation are shown in Fig. S4, indicating significant differences between the two types of electrodes in terms of their corresponding cellular immune responses. In the early stage of implantation, due to the intrinsic immune responses, microglial cells were found to aggregate around electrodes, and the synaptic contraction were observed from morphological studies, indicating the activation of the microglial cells. This would subsequently promote the activation of the neighboring astrocytes. Comparing the morphologies of microglial cells around both types of electrodes, there is significantly less aggregation of microglial cells around bio-array electrodes than metal electrodes. With the increasing of implantation time, a superior glial cell aggregation was observed around metal electrodes, and the size of astrocytes near the metal electrodes appeared larger as compared to those around the bio-array electrodes, which approved that the astrocytes near metal electrodes are continuously stimulated along with implantation. After 12 weeks of implantation, there was almost no astrocyte encapsulation around the bioelectrode, while a large number of hypertrophic astrocytes aggregated surrounding the metal electrode. This might be attributed to the presence of the 'transition layer' between the bioelectrode and brain tissue, forming a stable electrode-neural interface barrier after implantation. Such a 'transition layer' is composed of a biocompatible hydrogel material that generates lower immune reactions upon implantation, thereby reducing the stimulation level on astrocytes during early stages and inhibit their migration. Additionally, during long-term implantation, the small modulus difference between this 'transition layer' and brain tissue reduces mechanical damage caused by micromotion between the electrode and brain tissue, leading to decreased immune response in brain tissue and reduced glial scar formation over time. This phenomenon demonstrates that compared to metal array electrodes, bio-enhanced electrodes minimize the extent of scar formation after implantation. Moreover, the distribution of glial scars has a significant impact on signal quality, as shown in Fig. S6. The channels at the four central positions of the array electrode are referred to as inner channels, while the others are defined as

outer channels. For both metal array electrodes and bio-enhanced array electrodes, larger density of astrocytes can be found in the inner channels, and the signal intensity and the number of spike signals detected in the outer channels were higher than those in the inner channels. This observation aligns with the phenomenon depicted in Fig. 7A, where the degree of glial encapsulation around the inner channels of the bio-enhanced array electrodes was greater than that around the outer channels. This can be attributed to the migration and aggregation of astrocytes around the electrodes.

It has been reported that after 4 weeks of electrode implantation, there is a significant increase in the number of astrocytes in the tissue and an increase in the thickness of the fibrous sheath [50]. This supports the idea that long-term implantation of electrodes in the body can stimulate chronic inflammation, leading to changes in neural tissue and fibrous encapsulation around the electrode. The generation of chronic inflammatory response is a complex biological process involving interactions between various immune cells and release of inflammatory mediators. After electrode implantation, the body quickly responds by attracting macrophages to the implant site, which secrete various pro-inflammatory factors such as interleukins and tumor necrosis factor, initiating hypertrophy and proliferation processes in astrocytes. Ultimately, macrophages, astrocytes, oligodendrocytes, and microglia near the electrode form a fibrous sheath together. The increased fibrous sheath surrounding the electrode surface increases impedance and reduces electrode performance [51–53]. In addition, biochemical factors with neurotoxicity such as prostaglandins, TNF-α, and IL-1β generated as the result of immune responses can damage or even kill surrounding neurons, causing a significant drop in the number of stimulated or recorded neurons, and subsequently leads to weakened or even failed electrode functionality. These previous findings corroborate our experimental results which showed a gradual decrease in signal acquisition capability of the metal electrodes.

Despite its contributions, this study has certain limitations. First, there is room for improvement in the manufacturing precision of the electrode's bio-coating. The uniformity of the bio-coating thickness may affect key properties such as conductivity and bioactivity of the electrodes. Second, the investigation of the long-term stability and biointegration performance of the elelectrodes was limited to *in vivo* monitoring for three months. Extended studies exceeding one year could provide a more robust foundation for evaluating the tissue compatibility of this design. Furthermore, while the *in vivo* results effectively demonstrated the stability of high biointegration and high-quality signal detection in the bio-array electrodes, systematic studies on the overall degradation mechanisms of the bio-coating and its interface integration performance may well be needed. Compared to metal electrodes, the bioelectrodes developed in this study exhibited similar levels of glial encapsulation in the short term after electrode implantation, indicating that both types of electrodes induce short-term inflammatory responses, and subsequently reduce the accuracy of signal monitoring.

5. Conclusions

This study addresses the challenge of improving the bio-adaptability of implantable neural electrodes with brain tissue by proposing a novel bio-enhanced coating structure for neural electrodes. Through a combination of numerical simulations and experimental validations, the structure, materials, and performance of the electrodes were optimized. Both *in vitro* and *in vivo* experiments demonstrated the effectiveness of the bio-enhanced design in improving the long-term biocompatibility and electrical signal acquisition capabilities of the electrodes. The main conclusions are as follows:

1) A novel bio-enhanced neural electrode design with a heterogeneous transition layer structure was proposed. An optimized array electrode design was developed to improve the signal acquisition range and spatial resolution without increasing electrode size, resolving the trade-off between electrode flexibility and implantation performance.
2) A bio-conductive gel coating material combining polyaniline, gelatin, and sodium alginate was developed, demonstrating a modulus similar to brain tissue, excellent biocompatibility for neural cell proliferation, and electrical conductivity suitable for electrode applications. This material effectively reduced the mechanical mismatch at the electrode-tissue interface, enhancing biointegration while maintaining electrical performance.
3) A bio-array electrode was fabricated based on the optimized coating processing and the array site design. The bio-conductive coating improved the charge transfer capacity (1.74-fold increase) and reduced impedance (63.17 %) compared to uncoated electrodes. The array design maintained high signal recording quality while increasing the number of channels, exhibiting excellent electrochemical performance and stability.
4) Long-term *in vivo* experiments validated the bio-enhanced neural electrode's performance. After 12 weeks of implantation, the bio-array electrodes caused significantly less brain tissue damage (101 ±7 μm, 1/4 of metal electrodes) and reduced astrocyte scarring (62 ± 34 μm). The array electrode demonstrated stable recording of neural signals over 60 days, with superior SNR compared to metal electrodes (2.1-folds higher for action potentials). An optimized 200 μm electrode spacing was shown to balance signal quality and recording range, achieving enhanced biointegration and fusion with neural tissue.

In summary, the proposed bio-array electrodes design effectively improves the biocompatibility, mechanical adaptability, and electrical performance of implantable electrodes, providing a promising solution for long-term neural interfacing applications.

CRediT authorship contribution statement

Ling Wang: Writing – review & editing, Writing – original draft, Methodology, Funding acquisition, Data curation. **Chenrui Zhang:** Writing – review & editing, Writing – original draft, Software, Methodology, Investigation, Formal analysis, Data curation. **Zhiyan Hao:** Writing – review & editing, Investigation. **Siqi Yao:** Writing – review & editing, Software. **Luge Bai:** Methodology. **Joaquim Miguel Oliveira:** Investigation. **Pan Wang:** Resources. **Kun Zhang:** Investigation. **Chen Zhang:** Supervision. **Jiankang He:** Validation. **Rui L. Reis:** Investigation. **Dichen Li:** Writing – review & editing.

Ethics approval and consent to participate

The use and care of experimental animals were approved by the Biomedical Ethics Committee of the Xi'an Jiaotong University Health Science Center (approval No. 2022-15), in compliance with all relevant ethical regulations.

Declaration of competing interest

Rui L. Reis is an associate editor for Bioactive Materials and was not involved in the editorial review or the decision to publish this article. There is no conflict of interests involved in this study.

Acknowledgements

The work was supported by the Program of the National Natural Science Foundation of China [52275291], [52435006], the Program for Innovation Team of Shaanxi Province (2023-CX-TD-17), and the Fundamental Research Funds for the Central Universities.

Appendix A. Supplementary data

Supplementary data to this article can be found online at https://doi.org/10.1016/j.bioactmat.2024.12.033.

References

[1] N. Wu, S. Wan, S. Su, et al., Electrode materials for brain-machine interface: a review, InfoMat 3 (11) (2021) 1174–1194, https://doi.org/10.1002/inf2.12234.

[2] B. Wodlinger, J.E. Downey, E.C. Tyler-Kabara, et al., Ten-dimensional anthropomorphic arm control in a human brain-machine interface: difficulties, solutions, and limitations, J. Neural. Eng. 12 (1) (2015) 016011, https://doi.org/10.1088/1741-2560/12/1/016011.

[3] K.M. Szostak, L. Grand, T.G. Constandinou, Neural interfaces for intracortical recording: requirements, fabrication methods, and characteristics, Front. Neurosci. 11 (2017) 665–675, https://doi.org/10.3389/fnins.2017.00665.

[4] J. Rivnay, H. Wang, L. Fenno, et al., Next-generation probes, particles, and proteins for neural interfacing, Sci. Adv. 3 (6) (2017) 56–75, https://doi.org/10.1126/sciadv.1601649.

[5] N. Obidin, F. Tasnim, C. Dagdeviren, The future of neuroimplantable devices: a materials science and regulatory perspective, Adv. Mater. 32 (15) (2020) 1901482, https://doi.org/10.1002/adma.201901482.

[6] E. Musk, Neuralink, An integrated brain-machine interface platform with thousands of channels, J. Med. Internet Res. 21 (10) (2019) e16194, https://doi.org/10.2196/16194.

[7] N.A. Steinmetz, C. Aydin, A. Lebedeva, et al., Neuropixels 2.0: a miniaturized high-density probe for stable, long-term brain recordings, Science 372 (6539) (2021) eabf4588, https://doi.org/10.1126/science.abf4588.

[8] N. Chen, L. Tian, A.C. Patil, et al., Neural interfaces engineered via micro- and nanostructured coatings, Nano Today 14 (2017) 59–83, https://doi.org/10.1016/j.nantod.2017.04.007.

[9] T.L. Massey, S.R. Santacru, J.F. Hou, et al., A high-density carbon fiber neural recording array technology, J. Neural. Eng. 16 (1) (2019) 785–791, https://doi.org/10.1088/1741-2552/aae8d9.

[10] J.E. Chung, H.R. Joo, J.L. Fan, et al., High-density, long-lasting, and multi-region electrophysiological recordings using polymer electrode arrays, Neuron 101 (1) (2019) 21–36, https://doi.org/10.1016/j.neuron.2018.11.002.

[11] G. Hong, C.M. Lieber, Novel electrode technologies for neural recordings, Nat. Rev. Neurosci. 20 (6) (2019) 330–345, https://doi.org/10.1038/s41583-019-0140-6.

[12] J. Liu, C. Xie, X. Dai, et al., Multifunctional three-dimensional macroporous nanoelectronic networks for smart materials, Proc. Natl. Acad. Sci. U.S.A. 110 (17) (2013) 6694–6699, https://doi.org/10.1073/pnas.1305209110.

[13] P.B. Kruskal, Z. Jiang, T. Gao, et al., Beyond the patch clamp: nanotechnologies for intracellular recording, Neuron 86 (1) (2015) 21–24, https://doi.org/10.1016/j.neuron.2015.01.004.

[14] M. Vomero, F. Ciarpella, E. Zucchini, et al., On the longevity of flexible neural interfaces: establishing biostability of polyimide-based intracortical implants, Biomaterials 281 (2022) 121372, https://doi.org/10.1016/j.biomaterials.2022.121372.

[15] M. Shin, J. Lim, J. An, et al., Nanomaterial-based biohybrid hydrogel in bioelectronics, Nano Convergence 10 (1) (2023) 4862, https://doi.org/10.1186/s40580-023-00357-7.

[16] S. Li, Y. Cong, J. Fu, Tissue adhesive hydrogel bioelectronics, J. Mater. Chem. B 9 (22) (2021) 4423–4443, https://doi.org/10.1039/D1TB00523E.

[17] Y. Zhou, H. Yang, X. Wang, et al., A mosquito mouthpart-like bionic neural probe, Microsyst. Nanoeng. 9 (1) (2023) 88, https://doi.org/10.1038/s41378-023-00565-5.

[18] Y. Zhou, C. Gu, J. Liang, et al., A silk-based self-adaptive flexible opto-electro neural probe, Microsyst. Nanoeng. 8 (6) (2022) 118, https://doi.org/10.1038/s41378-022-00461-4.

[19] A. Zhang, Y. Zhao, S.S. You, et al., Nanowire probes could drive high-resolution brain-machine interfaces, Nano Today 31 (2020) 100821, https://doi.org/10.1016/j.nantod.2019.100821.

[20] L. Luan, X. Wei, Z. Zhao, et al., Ultraflexible nanoelectronic probes form reliable, glial scar-free neural integration, Sci. Adv. 3 (2) (2017) 4682, https://doi.org/10.1126/sciadv.1601966.

[21] E. Masvidal-Codina, X. Illa, M. Dasilva, et al., High-resolution mapping of infraslow cortical brain activity enabled by graphene microtransistors, Nat. Mater. 18 (3) (2019) 280–296, https://doi.org/10.1038/s41563-018-0249-4.

[22] D.C. Kim, H.J. Shim, W. Lee, et al., Material-based approaches for the fabrication of stretchable electronics, Adv. Mater. 32 (15) (2020) 325412, https://doi.org/10.1002/adma.201902743.

[23] J. Liu, X. Zhang, Y. Liu, et al., Intrinsically stretchable electrode array enabled *in vivo* electrophysiological mapping of atrial fibrillation at cellular resolution, Proc. Natl. Acad. Sci. U.S.A. 117 (26) (2020) 14769–14778, https://doi.org/10.1073/pnas.2000207117.

[24] M. Vosgueritchian, D.J. Lipomi, Z. Bao, Highly conductive and transparent PEDOT:PSS films with a fluorosurfactant for stretchable and flexible transparent electrodes, Adv. Funct. Mater. 22 (2) (2012) 421–428, https://doi.org/10.1002/adfm.201101775.

[25] Y. Liu, J. Liu, S. Chen, et al., Soft and elastic hydrogel-based microelectronics for localized low-voltage neuromodulation, Nat. Biomed. Eng. 3 (1) (2019) 58–68, https://doi.org/10.1038/s41551-018-0335-6.

[26] S. Guan, J. Wang, X. Gu, et al., Elastocapillary self-assembled neurotassels for stable neural activity recordings, Sci. Adv. 5 (3) (2019) eaav2842, https://doi.org/10.1126/sciadv.aav2842.

[27] K.C. Spencer, J.C. Sy, K.B. Ramadi, et al., Characterization of mechanically matched hydrogel coatings to improve the biocompatibility of neural implants, Sci. Rep. 7 (2) (2017) 546668, https://doi.org/10.1038/s41598-017-02107-2.

[28] S. Park, H. Yuk, R. Zhao, et al., Adaptive and multifunctional hydrogel hybrid probes for long-term sensing and modulation of neural activity, Nat. Commun. 12 (1) (2021) 528357, https://doi.org/10.1038/s41467-021-23802-9.

[29] M. Yao, Z. Wei, J. Li, et al., Microgel reinforced zwitterionic hydrogel coating for blood-contacting biomedical devices, Nat. Commun. 13 (1) (2022) 452347, https://doi.org/10.1038/s41467-022-33081-7.

[30] J. Xiong, B. Zhang, A. Balilonda, et al., Graphene-based implantable neural electrodes for insect flight control, J. Mater. Chem. B 10 (24) (2022) 4632–4639, https://doi.org/10.1039/D2TB00906D.

[31] C. Tang, S. Xie, M. Wang, et al., A fiber-shaped neural probe with alterable elastic moduli for direct implantation and stable electronic-brain interfaces, J. Mater. Chem. B 8 (20) (2020) 4387–4394, https://doi.org/10.1039/D0TB00508H.

[32] H.B. Li, J.F. Wang, Y. Fang, Recent developments in multifunctional neural probes for simultaneous neural recording and modulation, Microsyst. Nanoeng. 9 (1) (2023) 4, https://doi.org/10.1038/s41378-022-00444-5.

[33] C. Gu, J. Jiang, T.H. Tao, et al., Long-term flexible penetrating neural interfaces: materials, structures, and implantation, Sci. China Inf. Sci. 64 (12) (2021) 1–18, https://doi.org/10.1007/s11432-021-3321-7.

[34] M. Beygisangchin, S.A. Rashid, S. Shafie, et al., Preparations, properties, and applications of polyaniline and polyaniline thin films-A review, Polymers 13 (12) (2021) 2003, https://doi.org/10.3390/polym13122003.

[35] J. Wang, T. Wang, H. Liu, et al., Flexible electrodes for brain-computer interface system, Adv. Mater. (2023) 2211012, https://doi.org/10.1002/adma.202211012.

[36] R.A. Green, S. Baek, L.A. Poole-Warren, et al., Conducting polymer-hydrogels for medical electrode applications, Sci. Technol. Adv. Mater. 6 (8) (2010) 63–95, https://doi.org/10.1088/1468-6996/11/1/014107.

[37] Z. Zhang, G. Tian, X. Duan, et al., Nanostructured PEDOT coatings for electrode-neuron integration, ACS Appl. Bio Mater. 4 (7) (2021) 5556–5565, https://doi.org/10.1021/acsabm.1c00375.

[38] L.-P. Wang, W. Wang, L. Di, et al., Protein adsorption under electrical stimulation of neural probe coated with polyaniline, Colloids Surf. B Biointerfaces 80 (1) (2010) 72–78, https://doi.org/10.1016/j.colsurfb.2010.05.034.

[39] L. Di, L.P. Wang, Y.N. Lu, et al., Protein adsorption and peroxidation of rat retinas under stimulation of a neural probe coated with polyaniline, Acta Biomater. 7 (10) (2011) 3738–3745, https://doi.org/10.1016/j.actbio.2011.06.009.

[40] Y. Wang, M. Han, L. Jing, et al., Enhanced neural activity detection with microelectrode arrays modified by drug-loaded calcium alginate/chitosan hydrogel, Biosens. Bioelectron. 267 (2024) 116837, https://doi.org/10.1016/j.bios.2024.116837.

[41] B.A. Olshausen, Theoretical neuroscience: computational and mathematical modeling of neural systems, J. Cognit. Neurosci. 15 (1) (2003) 154–155. https://api.semanticscholar.org/CorpusID:14072069.

[42] I. Bružauskaitė, D. Bironaitė, E. Bagdonas, et al., Scaffolds and cells for tissue regeneration: different scaffold pore sizes—different cell effects, Cytotechnology 68 (3) (2016) 355–369, https://doi.org/10.1007/s10616-015-9895-4.

[43] S.F. Cogan, Neural stimulation and recording electrodes, Annu. Rev. Biomed. Eng. 10 (1) (2008) 275–309, https://doi.org/10.1146/annurev.bioeng.10.061807.160518.

[44] B. Shen, X. Liao, X. Hu, et al., A hollow nano-flower NiCo2O4@Nb2CTx MXene heterostructure via interfacial engineering for high-performance flexible supercapacitor electrodes, J. Mater. Chem. A 11 (31) (2023) 16823–16837, https://doi.org/10.1039/D3TA02729E.

[45] B. Lu, H. Yuk, S. Lin, et al., Pure PEDOT:PSS hydrogels, Nat. Commun. 10 (1) (2019) 45–62, https://doi.org/10.1038/s41467-019-09003-5.

[46] D. Lou, C. Wang, Z. He, et al., Robust organohydrogel with flexibility and conductivity across the freezing and boiling temperatures of water, Chem. Commun. 55 (58) (2019) 8422–8425, https://doi.org/10.1039/C9CC04239C.

[47] M. Leber, R. Bhandari, J. Mize, et al., Long term performance of porous platinum coated neural electrodes, Biomed. Microdevices 19 (3) (2017) 32–53, https://doi.org/10.1007/s10544-017-0201-4.

[48] G.K.K. Chik, N. Xiao, X. Ji, et al., Flexible multichannel neural probe developed by electropolymerization for localized stimulation and sensing, Advanced Materials Technologies 7 (8) (2022) 2200143, https://doi.org/10.1002/admt.202200143.

[49] T. Hyakumura, U. Aregueta-Robles, W. Duan, et al., Improving deep brain stimulation electrode performance *in vivo* through use of conductive hydrogel coatings, Front. Neurosci. 15 (2021) 761525, https://doi.org/10.3389/fnins.2021.761525.

[50] R. Biran, D.C. Martin, P.A. Tresco, Neuronal cell loss accompanies the brain tissue response to chronically implanted silicon microelectrode arrays, Exp. Neurol. 195 (1) (2005) 115–126, https://doi.org/10.1016/j.expneurol.2005.04.020.

[51] X. Jin, T. Yamashita, Microglia in central nervous system repair after injury, J. Biochem. 159 (5) (2016) 491–496, https://doi.org/10.1093/jb/mvw009.

[52] V.S. Polikov, P.A. Tresco, W.M. Reichert, Response of brain tissue to chronically implanted neural electrodes, J. Neurosci. Methods 148 (1) (2005) 1–18, https://doi.org/10.1016/j.jneumeth.2005.08.015.

[53] G.C. Mcconnell, T.M. Schneider, D.J. Owens, et al., Extraction force and cortical tissue reaction of silicon microelectrode arrays implanted in the rat brain, IEEE Trans. Biomed. Eng. 54 (6) (2007) 1097–1107, https://doi.org/10.1109/TBME.2007.895373.